Solar Energy 198 (2020) 151–159

Contents lists available at ScienceDirect

Solar Energy

journal homepage: www.elsevier.com/locate/solener

Boosting the cost-effectiveness of luminescent solar concentrators through subwavelength sanding treatment

Yilin Li[a,b,*], Yujian Sun[a,c], Yongcao Zhang[d]

[a] Solera City Energy, Harbin, Heilongjiang 150000, China
[b] Department of Chemical and Biomolecular Engineering, Rice University, Houston, TX 77005, United States
[c] School of Environmental and Forest Sciences, University of Washington, Seattle, WA 98195, United States
[d] Department of Mechanical Engineering, University of Houston, Houston, TX 77004, United States

ARTICLE INFO

Keywords:
Luminescent solar concentrator
Cost-effectiveness
Subwavelength sanding treatment
Commercialization
Power conversion efficiency
Power concentration ratio

ABSTRACT

In this report, we introduced subwavelength sanding treatment to boost the cost-effectiveness of luminescent solar concentrators (LSCs). It was proven the hypothesis that sanding the device surface to roughness (R_q = 22–105-nm) much smaller than the wavelength of sunlight (λ = 280–4000 nm) would improve the device performance due to much higher scattering gain than scattering loss. Experimental results showed that the sanded devices exhibited power conversion efficiency (η_{LSC}) and power concentration ratio (C) enhanced by at least 44% and could have the doping concentration of the luminophores significantly reduced by 87.5%. Measurement on the waveguide edge emission revealed that the performance enhancement was attributed to the utilization of the long-wavelength (λ > 800 nm) photons. Monte Carlo ray tracing simulation signified that the subwavelength sanding treatment was also applicable to large-area devices with geometric gain (G) up to 120 (9.29 m^2) and devices made of other luminophores. Cost-effectiveness analysis indicated a huge reduction by 45% in the price per watt (*PPW*) for large-area commercial-sized (80 in. by 40 in.) LSCs. This study suggested that subwavelength sanding treatment was promising to bridge the gap between research and commercialization of the LSCs.

1. Introduction

Although the concept of luminescent solar concentrator (LSC) is introduced in 1970s (Weber and Lambe, 1976; Goetzberger and Greube, 1977), the research of LSC is now being paid much more attention than ever before because LSCs are considered promising for building-integrated photovoltaic (BIPV) technology (van Sark et al., 2008; Debije and Verbunt, 2012), which is widely emphasized in the distributed renewable energy deployment. The use of LSCs to transform exterior building parts such as windows, facades and atriums into energy-harvesting devices enables the possibility to harvest solar energy almost everywhere within our community (Kerrouche et al., 2014; Sark et al., 2017) (Fig. 1a). The typical design of LSC consists of a slab-shaped waveguide doped with luminophores and solar cells attached to the edge of the waveguide. The typical operation of LSC is that short-wavelength photons in the sunlight are absorbed by the luminophores and converted into long-wavelength photons, which follow successive total internal reflection (TIR) inside the waveguide and eventually transport to the edge-attached solar cells (Fig. 1b) (Batchelder et al., 1979; Batchelder et al., 1981; Li et al., 2019). Studies have shown that LSCs can work efficiently under different light conditions (Debije and Rajkumar, 2015; Li et al., 2019) and can be fabricated with different colors or even transparency (Zhao and Lunt, 2013; Zhao et al., 2014; Yang et al., 2018). The unique features of generating electricity while being aesthetically pleasing have suggested huge potential of LSCs to be applied in the built environment where it has proven difficult to deploy conventional solar panels (Chau et al., 2010).

Numerous efforts have been taken to improve the performance of LSCs over the past several years. There is no doubt that searching for luminophores with ideal spectroscopic properties is one of the major tasks. A large number of luminophores have been developed in the categories of organic dyes (Sanguineti et al., 2013; Mouedden et al., 2015; Li et al., 2016), quantum dots (Purcell-Milton and Gun'ko, 2012; Zhou et al., 2018; Moraitis et al., 2018) and rare-earth complexes (Liu et al., 2014; Freitas et al., 2015; Frias et al., 2019). Several improvements have been made to the spectroscopic properties of luminophores, including absorption and emission spectra, spectral overlap and photoluminescence quantum yield (PLQY). Some luminophores are

* Corresponding author at: Department of Chemical and Biomolecular Engineering, Rice University, Houston, TX 77005, United States.
E-mail address: yilinli@rice.edu (Y. Li).

https://doi.org/10.1016/j.solener.2020.01.038
Received 7 December 2019; Received in revised form 6 January 2020; Accepted 14 January 2020

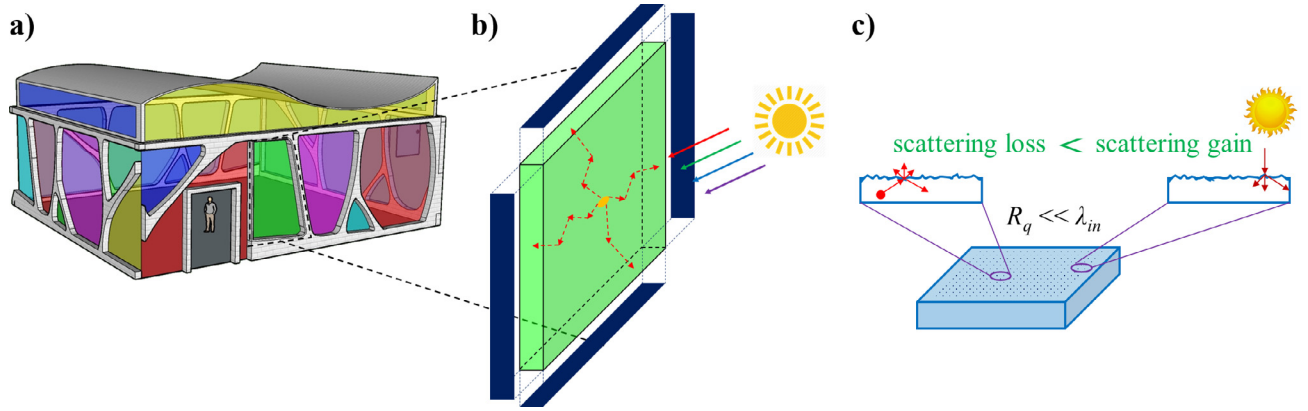

Fig. 1. Schematic representations of (a) the potential building application of LSCs, (b) the operational mechanism of an LSC, and (c) the concept of this study.

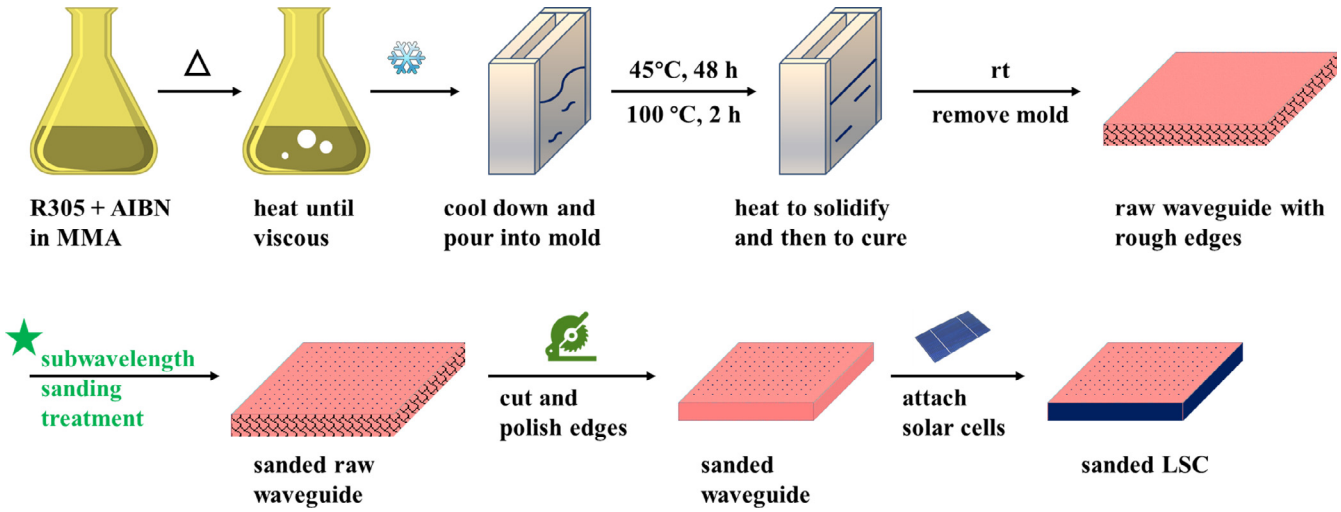

Fig. 2. Schematic representations of the fabrication of process of a sanded LSC.

designed with wide absorption range, which covers the solar spectrum up to the band gap of solar cell (Shcherbatyuk et al., 2010; Meinardi et al., 2015; Zhou et al., 2016). Others exhibit red-shifted emission, which matches the band gap of solar cell (Sanguineti et al., 2012; Chen et al., 2017; Yang et al., 2019). The self-absorption issue is tackled by luminophores with minimal spectral overlaps (Wang et al., 2011; Kate et al., 2015; Meinardi et al., 2017), and the photon loss is addressed by those with near-unity PLQYs (Knowles et al., 2015; Zhang et al., 2018; Bergren et al., 2018). Besides developing luminophores, imparting light management capability to LSCs is another focus. Various techniques have been explored to maximize the photon collection and concentration efficiency of LSCs. For example, the front surface of the waveguide is modified with optical microlens (Tseng et al., 2011; Damrongsak and Locharoenrat, 2017; Kurmi et al., 2018) or plasmonic structures (Chandra et al., 2012; Tummeltshammer et al., 2013; Fahad et al., 2017) to increase the intensity of the incidence. Wavelength-selective mirrors (Debije et al., 2010; Verbunt et al., 2012; Connell et al., 2018) and distributed Bragg reflectors (Xu et al., 2016; Connell and Ferry, 2016; Iasilli et al., 2019) are implemented to improve the photon trapping efficiency. There are also studies on the performance of large-area LSCs in different indoor and outdoor conditions to push forward the practical applications of the LSCs. Devices have been configured as office windows (Vossen et al., 2016), greenhouse panels (Corrado et al., 2016), and noise barriers (Kanellis et al., 2017; Debije et al., 2017; Debije et al., 2017).

Current studies on LSCs focus mostly on performance enhancement while there are handful reports on the improvement of cost-effectiveness (Sutherland et al., 2018). However, it is indeed very crucial for LSCs to demonstrate competitively high cost-effectiveness as a prerequisite for commercialization. In this report, we introduce a simple, low-cost and universal approach to boosting the cost-effectiveness of LSCs. Subwavelength sanding treatment was applied to the LSCs to achieve surface roughness much smaller than the wavelength of solar photons and thus to introduce photon scattering over the entire incident spectrum. Though increasing the surface roughness disturbs the photon transport and leads to photon loss during the successive TIR (i.e., scattering loss), it allows photons that are not absorbed by the luminophores to be utilized for power generation (i.e., scattering gain) (Fig. 1c). Our results showed that proper subwavelength sanding treatment led to much higher scattering gain than the scattering loss. Thus, the sanded devices collected much more photons than the unsanded devices, and surprisingly they required much less luminophores, implying significant cost reduction.

2. Experimental

2.1. Device fabrication

The fabrication of LSCs was according to the literature (Li et al., 2016) (Fig. 2). The procedure shown herein used 60 ppm luminophores and fabricated LSCs with an optical density (*OD*) of 4.0. For making LSCs with a low *OD*, decreasing the concentration of luminophores proportionally. In detail, luminophores (R305, TCI America) (Wilson et al., 2010; Sala et al., 2019; Griffini et al., 2013) and 0.1 w/w% radical initiator (azobisisobutyronitrile, Sigma-Aldrich) were dissolved in monomer (methyl methacrylate, MMA, Sigma-Aldrich) in an

Erlenmeyer flask. The solution was stirred in a water bath at 85 °C until the viscosity was close to glycerol. The heating was stopped, and the flask was placed in an ice/water bath at 0 °C. After being cooled down, the syrup was poured into a glass mold, which was placed in an incubator at 45 °C for 48 h for solidification. The mold was transferred to an oven and heated at 100 °C for 2 h. After being cooled down, the raw luminophore-doped poly(methyl methacrylate) (PMMA) slab can be easily separated from the mold. Subwavelength sanding treatment was then applied to front surface of the raw waveguides. The luminophore-doped waveguide was cut into square shape and the edges were polished. The thickness of the waveguide was 0.25 in., and the size was from 1 to 12 in., corresponding to the area from 6.45 cm^2 to 929 cm^2. Solar cells (polycrystalline silicon, p-Si, eBay) were then glued to the four edges of the waveguide using UV-curing optical adhesive. They were connected in parallel to maximize the device performance (Slooff et al., 2008). The detailed photovoltaic performance of solar cells was shown in our previous report (Li et al., 2019). Briefly, they exhibited averaged power conversion efficiency (η_{cell}) of 15.6% with short circuit current density (J_{sc}) of 330 $A{\cdot}m^{-2}$, open circuit voltage (V_{oc}) of 0.62 V and fill factor (*FF*) of 0.76.

2.2. Instrumentation

A homemade wind tunnel was used to perform the subwavelength sanding treatment. Its specifications and the experimental setup were given in the Appendix A. Supplementary material. The specifications of the sands used in the experiment were size of 0.5 mm and weight of 30 g. Surface height images of the waveguides were obtained using a Bruker ICON Atomic Force Microscope (AFM) with non-contact mode. Reflection and transmission spectra of the waveguides were collected using a Varian Cary 5000 UV–Vis-NIR spectrophotometer. Haze spectra of the waveguides were collected using a BYK Gardner Haze spectrophotometer. For waveguides with size greater than 3 in., small pieces were cut from the waveguides to fit the sample chamber of the spectrophotometer. An OAI class AAA solar simulator was used to provide simulated AM1.5G sunlight. Power conversion efficiency (η_{LSC}) and power concentration ratio (*C*) of the LSCs were calculated from the J-V curves measured by a Keithley 2401 sourcemeter. The emission spectra at the edge of the waveguides were recorded on a Horiba FL3-21 fluorescence spectrophotometer.

3. Results and discussion

3.1. Surface roughness and visual performance

Before attaching the solar cells to the waveguides, we first looked at the relationship between the sanding duration of the subwavelength sanding treatment and the surface roughness of the waveguides. During the subwavelength sanding treatment, sands continuously hit the front surface of the waveguides, making the surface rough (Fig. 3a). The root-mean-square (RMS) surface roughness (R_q) of the unsanded waveguide was 15-nm, while it changed to 22-nm, 33-nm, 46-nm, 63-nm, 82-nm and 105-nm for the sanding duration of 160 s, 110 s, 80 s, 60 s, 40 s, and 30 s, respectively, which indicated that a shorter sanding duration leaded to a rough surface (Fig. 3b). The R_q was with ± 10% standard deviation after 5 runs, suggesting that the process was reproducible. We also examined the surface profile of the waveguides before and after subwavelength sanding treatment (Fig. 3c). The surface height image of the unsanded waveguide showed that the surface contained a great number of nano-sized islands. With the increase of R_q, the nano-sized islands gradually became micro-sized islands, and at large R_q, some islands connected to each other to form large islands.

We next evaluated the visual performance of the LSCs by examining the waveguides. Bare waveguides without luminophores were used to measure the reflectance (R) and haze (H) of the front surface, and the luminophore-doped waveguides (*OD* = 4.0, 60 ppm) were used to measure the transmittance (*T*) and *H* of the bottom surface. To obtain *R*, *T* and *H* of the waveguides, the corresponding spectra measured using spectrophotometers were averaged over AM1.5G solar photon spectrum:

$$X(R,\ T\ \ or\ \ H) = \frac{\int_{400\ \ nm}^{700\ \ nm} X(\lambda)\phi_{sun}(\lambda)d\lambda}{\int_{400\ \ nm}^{700\ \ nm} \phi_{sun}(\lambda)d\lambda} \quad (1)$$

where $X(\lambda)$ is the photon spectra of the waveguides for *R*, *T* or *H*, and $\phi_{sun}(\lambda)$ is the AM1.5G solar photon spectrum.

The measurements on the front surface of the bare waveguides indicated that *R* decreased while *H* increased with the increase of R_q, which was within expectation because a rougher surface had more diffusive reflection than specular reflection (Fig. 4a). The unsanded bare waveguides (R_q = 15-nm) exhibited *R* of 5.95% and *H* of 1.26%, suggestive of minimal scattering on the front surface. For sanded waveguides, *H* was higher than *R* when R_q was greater than 33-nm, signifying strong scattering. At R_q of 105-nm, *R* was only 0.03%, and *H* was significantly higher than *R* by over 18%, which showed that the appearance of bare waveguides was highly hazy. Similar results were also obtained in the measurements on the bottom surface of the luminophore-doped waveguides (*OD* = 4.0, 60 ppm), in which *T* decreased while *H* increased and reached to a plateau with the increase of *R* (Fig. 4b). The unsanded waveguides (R_q = 15-nm) exhibited *T* of 24.20% and *H* of 12.94%. Because minimal scattering was associated with the unsanded waveguides, the high *T* was from the photons that were not absorbed by the luminophores, and the high *H* was due to the emitted photons of the luminophores that escaped from the waveguides. For sanded waveguides, *H* was higher than *T* when R_q was greater than 33-nm, indicating that the waveguides turned from transparent to hazy primarily due to the scattering of the emitted photons of the luminophores. The overall results suggested that the visual performance of the LSCs was affected by the subwavelength sanding treatment. At higher R_q, the appearance of the devices was hazier and less transparent. However, this would not limit the application of the LSCs in BIPV technology. Actually, this would broaden the application the LSCs. For example, devices with reduced reflection, reduced transparency and increased haze could be applied to some indoor places where privacy was required.

3.2. Size-dependent performance

We next attached solar cells to the waveguides and investigated the effect of R_q on the performance of the LSCs. The performance of the LSCs is described by two parameters (Li et al., 2016). The energy conversion capability of the device is represented by power conversion efficiency (η_{LSC}), which is the electric power produced by the device relative to the incident power, Higher η_{LSC} indicates more photons are converted to electric energy by the LSCs. The light concentration capability of the device is represented by power concentration ratio (*C*), which is the electric power produced by the solar cells attaching to the waveguide relative to the detached condition. LSCs with *C* greater than 1 suggest enhanced power output of the solar cells. In the study of the size-dependent performance, the size of the LSCs is described by geometric gain (*G*), which is the area of the front surface where photons are collected relative to the area of the edge where solar cells are attached. In this experiment, *G* was varied from 1 (6.45 cm^2) to 12 (929 cm^2) and the optical density (*OD*) of the waveguides, which is defined as the maximum absorption of the luminophore-doped waveguide, was kept consistent at 4.0 (60 ppm).

The relationship between η_{LSC} and *G* at different R_q was investigated first (Fig. 5a). A decreasing trend was observed for η_{LSC} with the increase of *G* despite R_q, indicating non-perfect photon transport inside the waveguide. This was because the transporting distance of the photons increased with the increase of *G*, which inevitably resulted in photon loss during successive TIR due to self-absorption of the

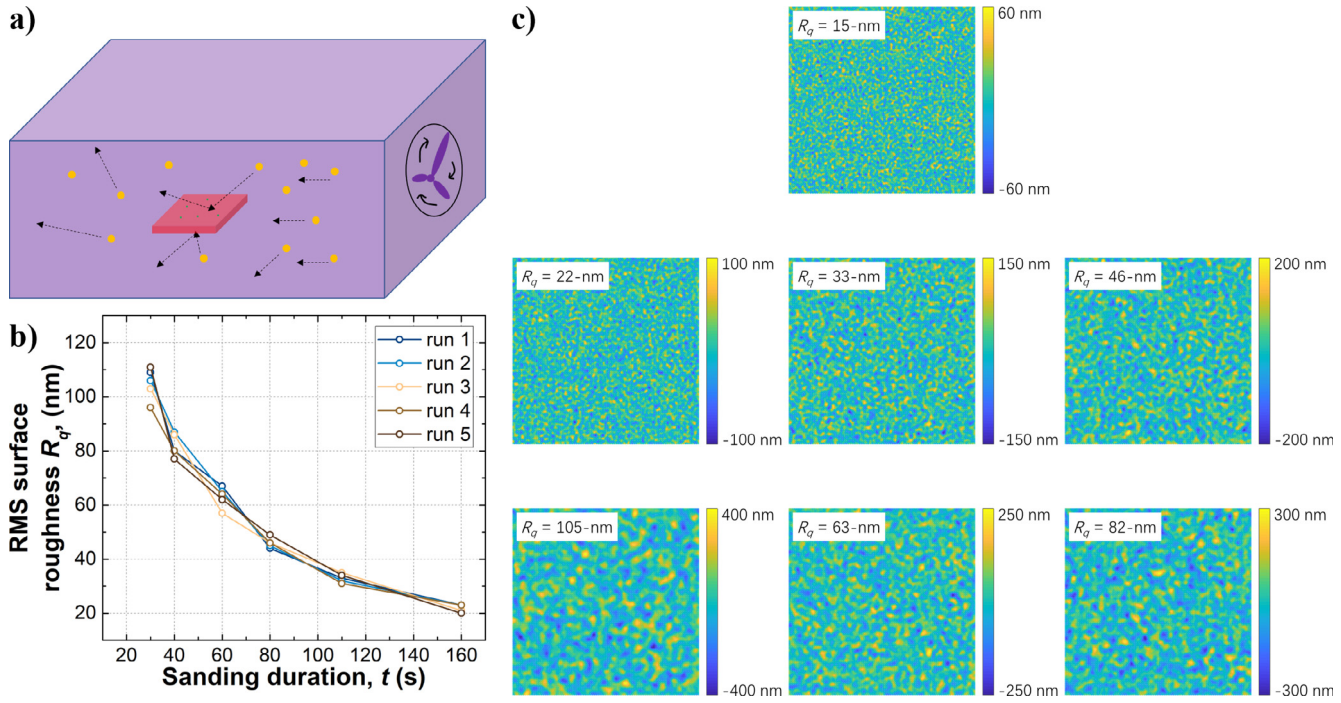

Fig. 3. (a) Schematic representation of an LSC under subwavelength sanding treatment, (b) relationship between sanding duration and R_q, and (c) surface height images (size: 5 μm × 5 μm).

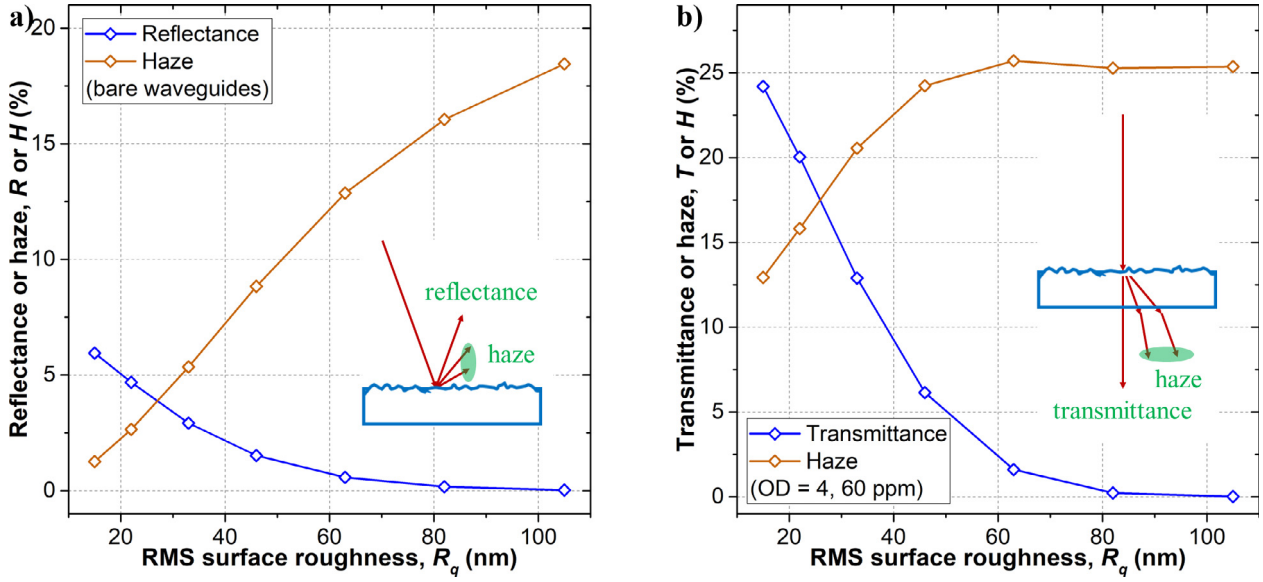

Fig. 4. The effect of R_q on (a) R and H of the front surface of the bare waveguides, and (b) T and H of the bottom surface of the luminophore-doped waveguides (OD = 4, 60 ppm).

luminophores as well as absorption and scattering of the waveguide. Moreover, η_{LSC} decreased rapidly with the increase of G when R_q increased. For example, η_{LSC} decreased by 19% (from 2.29% to 1.86%) at R_q = 15-nm, while it decreased by 54% (from 5.31% to 2.44%) at R_q = 105-nm. This was within the expectation because increasing R_q directly caused the increase of scattering of the waveguide, which interrupted the successive TIR. However, in this study, increasing R_q did not lead to η_{LSC} lower than its original value. For example, at G = 6 (232 cm^2), the sanded devices exhibited higher η_{LSC}, which ranged from the lowest value of 2.22% at R_q = 22-nm to the highest value of 3.29% at R_q = 82-nm, than the unsanded device, which exhibited η_{LSC} = 2.01% at R_q = 15-nm. The overall observed relationship between η_{LSC} and G at different R_q implied the balance between scattering gain and scattering loss. Optimal R_q was required to reach the maximum η_{LSC} at a given G. For example, the optimized R_q was 105-nm, 82-nm and 63-nm for G = 1 (6.45 cm^2), 6 (232 cm^2) and 12 (929 cm^2), respectively, which corresponded to the maximum η_{LSC} of 5.31%, 3.29% and 2.68%, respectively. The relationship between C and G was exactly opposite to that between on η_{LSC} and G, which showed that C increased with the increase of G at different R_q (Fig. 5b). Similarly, optimal R_q was required to reach the maximum C at a given G. For example, at G = 12 (929 cm^2), the optimal R_q was 63-nm, suggesting a sanded device (C = 2.06) output 44% more electrical power than the unsanded device (C = 1.43). For devices at a given G, the enhancement of η_{LSC} and C with increased R_q suggested the improvement of the cost-effectiveness of the LSCs after subwavelength sanding treatment.

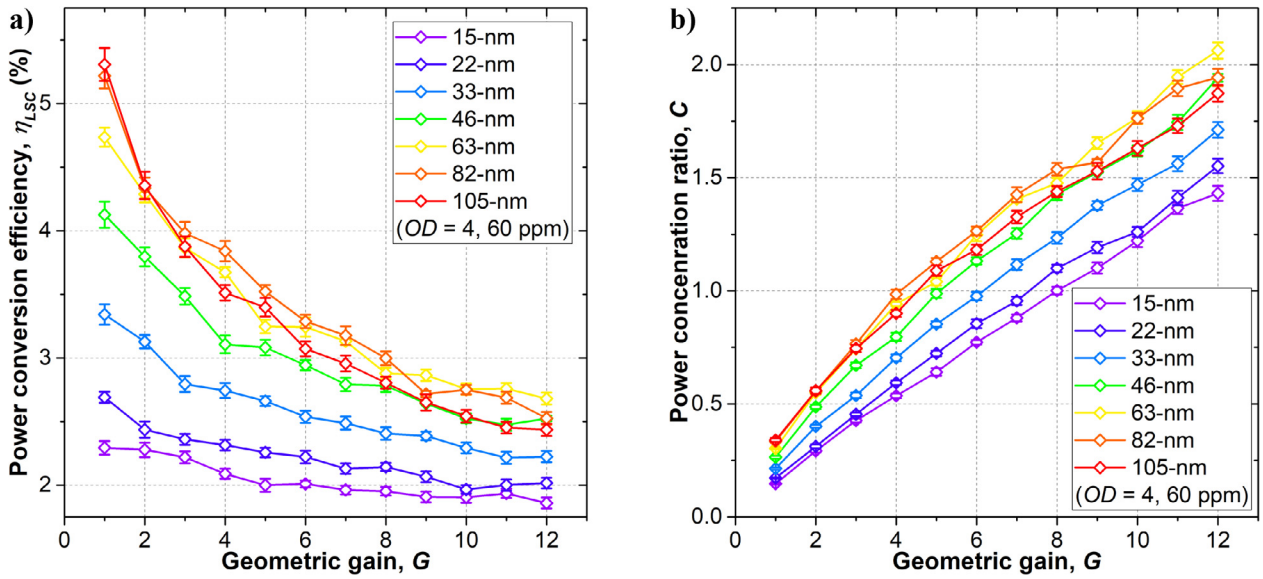

Fig. 5. The effect of R_q on the (a) η_{LSC} and (b) C of the LSCs (OD = 4, 60 ppm) with the increase of G.

3.3. Concentration-dependent performance

Our next study focused on the concentration-dependent performance of the LSCs at different R_q. In this experiment, devices with G of 6 (232 cm^2) and OD from 0.5 (7.5 ppm) to 4.0 (60 ppm) were investigated. The range of OD corresponded to the photon absorption at the absorption maximum of the luminophores from 68% to 99.99%. It was shown that after subwavelength sanding treatment, the devices exhibited enhancement in η_{LSC} by over 50% from below 2.1% to above 3.2% (Fig. 6a) and enhancement in C by over 50% from below 0.8 to above 1.2 (Fig. 6b). Moreover, the characteristic of performance enhancement was almost insensitive to OD. This suggested that the insufficient photon absorption due to the low doping concentration of the luminophores was compensated by the scattering gain from the subwavelength sanding treatment in the contribution to device performance. At R_q = 82-nm, the devices with OD of 0.5 (7.5 ppm) exhibited comparable performance (η_{LSC} = 3.23% and C = 1.24) to those with OD of 4.0 (60 ppm) (η_{LSC} = 3.31% and C = 1.27). In the former case, the use of the luminophores was significantly reduced by 87.5%, suggestive of a large cost reduction in the device fabrication, which led to significant improvement in cost-effectiveness of the LSCs.

3.4. Spectroscopic analysis on the edge emission

The performance improvement of the LSCs after subwavelength sanding treatment was considered attributable to an increased number of photons concentrated at the edge of the waveguide. To confirm this idea, we analyzed the edge emission of the waveguide with G of 6 (232 cm^2) and OD of 4.0 (60 ppm) at different R_q. To compare the results measured under different R_q, the relative emission spectrum was used, which was defined as the normalized measured emission spectrum at the edge of the waveguide ($I_{em}^{exp}(\lambda)$), followed by the multiplication with the short-circuit current of the edge-attached solar cells (I_{LSC}):

$$I_{em}(\lambda) = \frac{I_{em}^{exp}(\lambda)}{\int I_{em}^{exp}(\lambda)d\lambda} \times I_{LSC} \quad (2)$$

Before subwavelength sanding treatment on the device, the edge

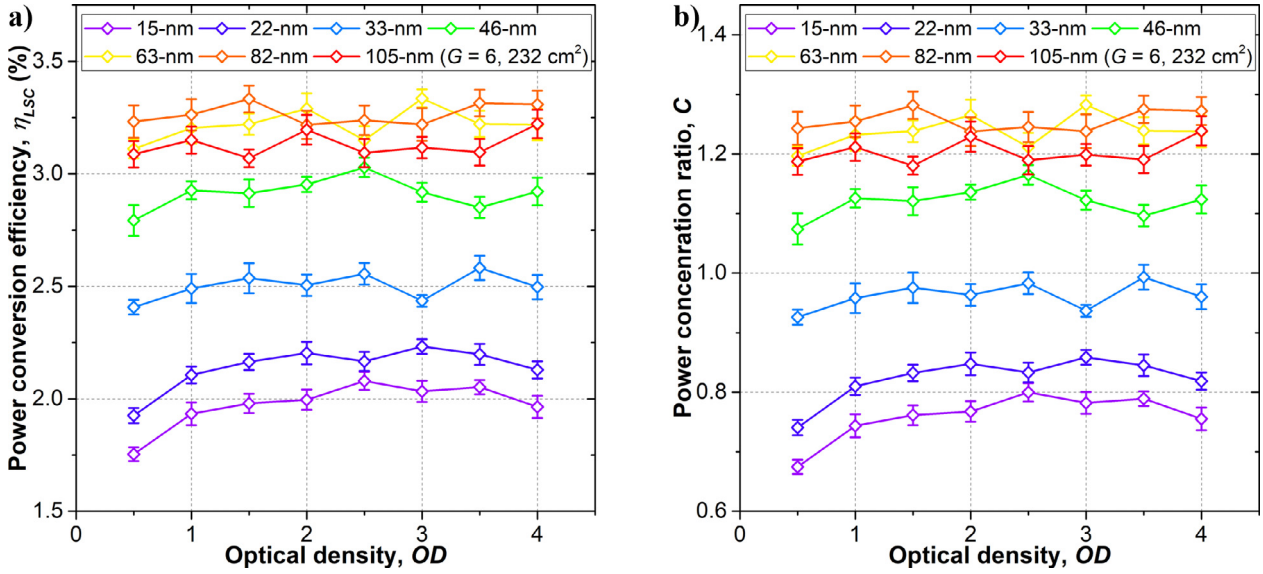

Fig. 6. The effect of R_q on the (a) η_{LSC} and (b) C of the LSCs (G = 6, 232 cm^2) with the increase of OD.

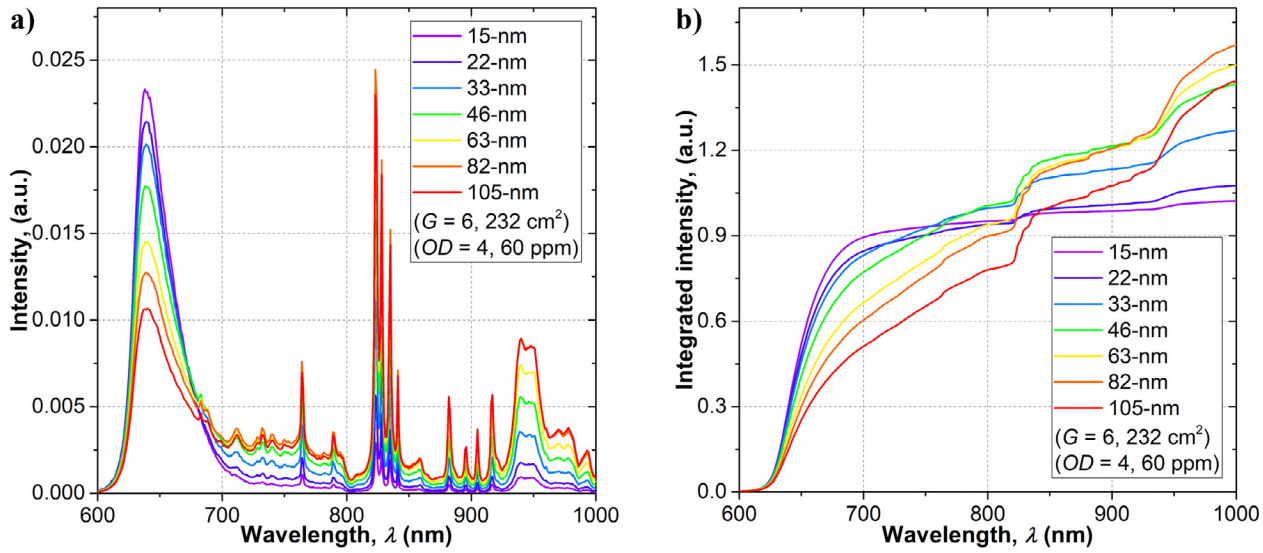

Fig. 7. (a) Edge emission spectra and (b) integrated intensity of the waveguides (G = 6, 232 cm^2 and OD = 4, 60 ppm) at different R_q.

emission exhibited a major peak at 638 nm, ascribing to the emission of the luminophores, and negligible discrete peaks at long wavelength (λ > 800 nm), ascribing to the scattering by the waveguide (Fig. 7a). After subwavelength sanding treatment of the device, the peak intensity at 638 nm decreased gradually with the increase of R_q, meanwhile the discrete peaks at λ > 800 nm emerged and the peak intensity increased rapidly. This observation indicated the balance between scattering gain and scattering loss. Since the scattering gain was much higher than the scattering loss, the overall effect resulted in the performance enhancement of the device. Moreover, the integrated intensity presented the balance between scattering gain and scattering loss from another point of view (Fig. 7b). Before λ = 800 nm, the scattering loss was the major portion, while after λ = 800 nm, it was suppressed by the scattering gain. The results of the integrated intensity at 1000 nm, which was near the band gap of the solar cells (i.e., Si, E_g = 1.12 eV), were consistent with those obtained from the size-dependent and concentration-dependent experiments.

3.5. Projected performance

The experimental results indicated that subwavelength sanding treatment was an effective approach to improving the performance of the LSCs with G up to 12 (929 cm^2). To explore whether this approach was also applicable to large-area devices, we performed Monte Carlo ray tracing simulation (Sahin et al., 2011; Leow et al., 2013; Shu et al., 2018) and obtained the projected η_{LSC} and C for devices with OD of 4.0 (60 ppm) and G up to 120 (9.29 m^2) (Fig. 8). The simulated values of η_{LSC} and C confirmed the experimental values when G was from 1 (6.45 cm^2) to 12 (929 cm^2), which suggested that it was reasonable to use the simulation to project the device performance at large areas. The trends of η_{LSC} and C with the increase of G up to 120 (9.29 m^2) at different R_q were consistent with previously observed trends when G was from 1 (6.45 cm^2) to 12 (929 cm^2). The projected results showed that R_q = 63-nm was the optimal value for maximizing performance in large-area devices with G > 12 (929 cm^2). For example, at the largest area where G = 120 (9.29 m^2), the maximum η_{LSC} was 1.47% and the maximum C was 9.58%, which were 11% higher than the values of η_{LSC} and C at R_q = 15-nm. The projected performance signified that subwavelength sanding treatment was applicable to large-area LSCs.

Besides the performance of large-area devices, we also simulated the performance of the devices (G = 6, 232 cm^2 and OD = 4.0, 60 ppm) made of other luminophores to verify that if the subwavelength sanding treatment was also effective. In the simulation, we used hypothetical luminophores, which had the same absorption and emission spectral shapes and Stokes shift as R305 (Li et al., 2019). The emission wavelength (λ_{em}) was made blue-shifted to 400 nm, 450 nm, 500 nm, 550 nm and 600 nm, and red-shifted to 650 nm and 700 nm, covering the visible region from 400 nm to 700 nm. As expected, enhancement in η_{LSC} and C were observed for the sanded devices (Fig. 9). Particularly, the devices made of luminophores with λ_{em} at short wavelength exhibited more significantly enhanced performance than those made of luminophores with λ_{em} at long wavelength. For example, for luminophores with λ_{em} of 400 nm, the device exhibited near 6-fold enhancement in η_{LSC} and C from η_{LSC} = 0.57% and C = 0.22 at R_q of 15-nm to η_{LSC} = 3.37% and C = 1.30 at R_q = 82-nm. The results showed that the subwavelength sanding treatment was a universal approach to the LSCs made of other luminophores.

3.6. Cost-effectiveness analysis

Our final study focused on the analysis of the cost-effectiveness of the LSCs without and with subwavelength sanding treatment. Here, the analysis was performed on hypothetical devices with the size of 80 in. by 40 in., equivalent to the typical size of a solar panel. Device 1 and 2 are unsanded devices (R_q = 15-nm) with OD of 0.5 (7.5 ppm) and 4.0 (60 ppm), respectively, while device 3 and 4 were device 1 and 2 with subwavelength sanding treatment (R_q = 63-nm), respectively. The Monte Carlo ray tracing method in the previous section was employed to estimate the η_{LSC}. The total cost of an LSC was estimated from the market price of the components, which primarily included the cost of optical waveguide (density: 1180 kg·m^{-3}; unit price: 3 \$·kg^{-1}; subtotal cost: \$46.4) (Unit price of optical waveguide, 2019), luminophores (absorption coefficient: 16 ppm·OD^{-1}; unit price: 50 \$·g^{-1}; subtotal cost: 12.4 \$·OD^{-1}) (Unit price of luminophores, 2019) and solar cells (unit price: 50 \$·m^{-2}; subtotal cost: \$1.9) (Unit price of solar cells, 2019). The total cost of an LSC with OD of 4.0 (60 ppm) was \$97.9 while the one with OD of 0.5 (7.5 ppm) was \$54.5. With the η_{LSC} and the cost of the LSCs known, price per watt (PPW) was calculated to describe the cost-effectiveness of the LSCs. The results showed that device 1, 2, 3 and 4 exhibited η_{LSC} of 1.61%, 1.92%, 1.92% and 1.96%, respectively (Fig. 10a). The corresponding PPW was 1.64 \$·W^{-1}, 2.47 \$·W^{-1}, 1.37 \$·W^{-1} and 2.42 \$·W^{-1}, respectively (Fig. 10b). For the unsanded devices, increasing the OD from 0.5 (7.5 ppm, device 1) to 4.0 (60 ppm, device 2) increased the η_{LSC} by 19%, but this significantly increased the PPW by 51% due to the significant increase of the amount of the luminophores. For the sanded devices (device 3 and 4), they

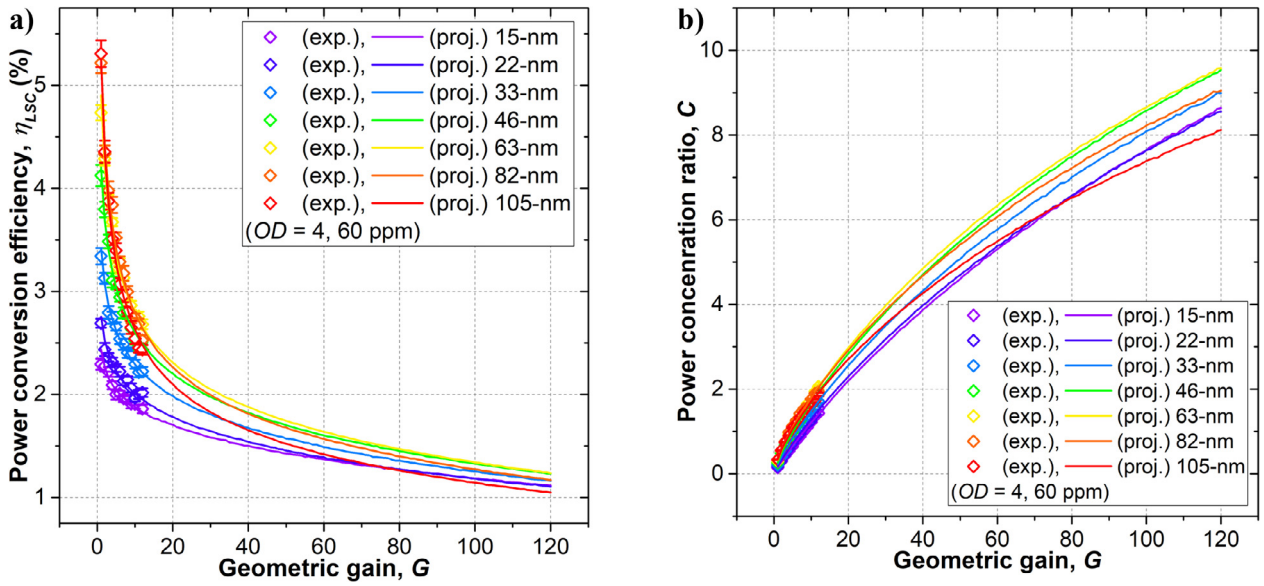

Fig. 8. Experimental (exp.) and projected (proj.) (a) η_{LSC} and (b) C of the LSCs (OD = 4) with G up to 120 (9.29 m^2) at different R_q.

exhibited comparable η_{LSC} but device 3 possessed a much lower *PPW* than device 4. The comparison between device 2 and device 4 suggested that the subwavelength sanding treatment may not be that effective to devices with a high *OD*. This was because scattering loss and scattering gain were balanced and did not lead to any performance improvement for the hypothetical device with a high *OD*. Nevertheless, high *OD* was not necessary for devices with subwavelength sanding treatment. The cost-effectiveness analysis conclusively signified that the subwavelength sanding treatment significantly reduced the *PPW* by 45% (from 2.47 \$·W^{-1} to 1.37 \$·W^{-1}) through the comparison between device 2 and 3, which possessed same η_{LSC} of 1.92%.

4. Conclusions

In summary, we applied subwavelength sanding treatment to the LSCs and found that R_q much less than the wavelength of the solar photons significantly improved the performance and reduced the cost of LSCs. First, the subwavelength sanding treatment made the device hazy, which broadened the application of LSCs in BIPV technology. Second, size-dependent study showed a minimal enhancement by 44% in η_{LSC} and C for devices with G up to 12 (929 cm^2) at R_q = 63-nm. Concentration-dependent study suggested that low-concentration sanded devices (OD = 0.5, 7.5 ppm and R_q = 82-nm) exhibited comparable performance to high-concentration unsanded devices (OD = 4.0, 60 ppm and R_q = 15-nm), which implied a huge cost reduction of the LSCs because the use of the luminophores was significantly reduced by 87.5%. Third, edge emission of the waveguide was analyzed to reveal the positive effect of the subwavelength sanding treatment, which was the utilization of long-wavelength (λ > 800 nm) photons. Monte Carlo ray tracing simulation signified that the subwavelength sanding treatment was also effective to large-area LSCs with G up to 120 (9.29 m^2) and devices made of other luminophores. Cost-effectiveness analysis indicated that the subwavelength sanding treatment led to significantly reduction in the *PPW* of the commercial-sized LSCs by 45%. It was attainable to have devices with high η_{LSC} of up to 1.92% and low *PPW* of down to 1.37 \$·W^{-1}. The subwavelength sanding treatment in this study was simple, low-cost and universal, and could be readily applied to any LSCs. This study would facilitate the

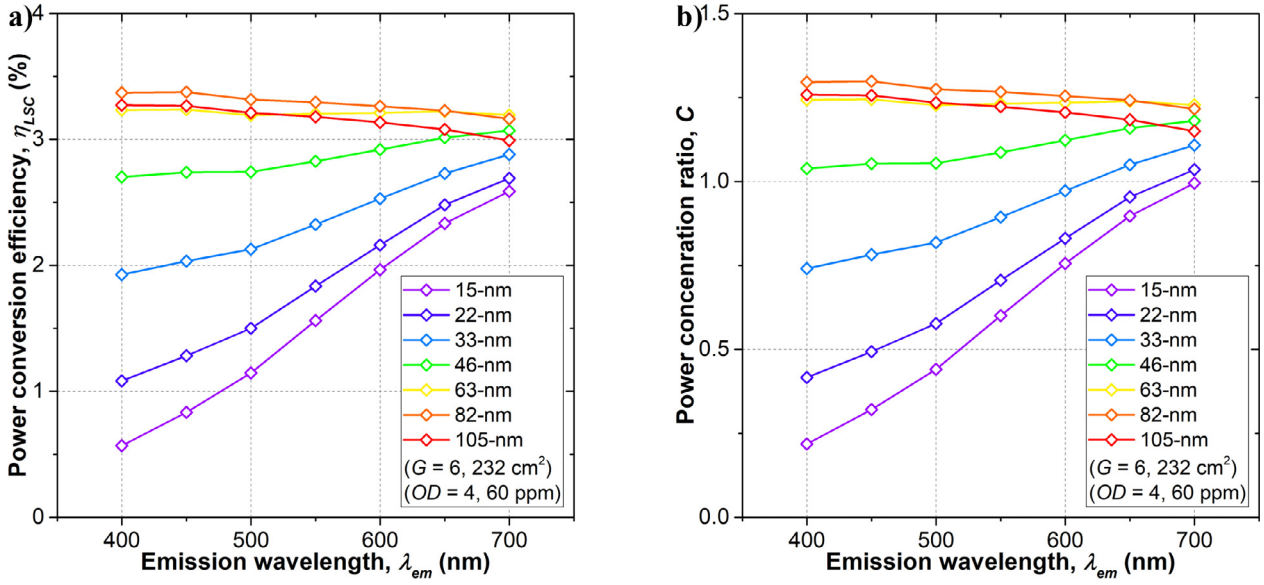

Fig. 9. The effect of R_q on the (a) η_{LSC} and (b) C of the LSCs (G = 6, 232 cm^2, OD = 4.0, 60 ppm) with the increase of λ_{em}.

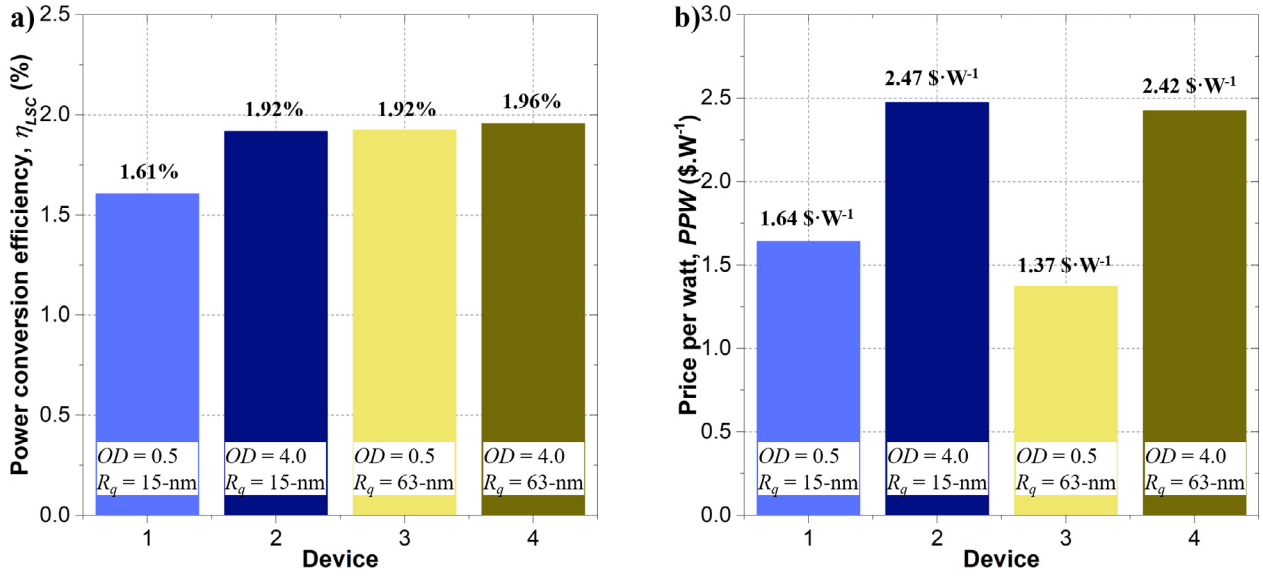

Fig. 10. (a) η_{LSC} and (b) *PPW* of the hypothetical LSCs with *OD* of 0.5 (7.5 ppm) and 4.0 (60 ppm) without and with subwavelength sanding treatment.

commercialization of the LSCs.

Declaration of Competing Interest

The authors declare that they have no known competing financial interests or personal relationships that could have appeared to influence the work reported in this paper.

Acknowledgement

The authors would like to thank Solera City Energy for financial support and the open-access research facilities at Rice University, University of Washington and University of Houston for instrumentation.

Appendix A. Supplementary material

Supplementary data to this article can be found online at https://doi.org/10.1016/j.solener.2020.01.038.

References

Weber, W.H., Lambe, J., 1976. Luminescent greenhouse collector for solar radiation. Appl. Opt. 15 (10), 2299–2300. https://doi.org/10.1364/ao.15.002299.
Goetzberger, A., Greube, W., 1977. Solar energy conversion with fluorescent collectors. Appl. Phys. 14 (2), 123–139. https://doi.org/10.1007/bf00883080.
van Sark, W.G.J.H.M., et al., 2008. Luminescent solar concentrators - a review of recent results. Opt. Express 16 (26), 21773–21792. https://doi.org/10.1364/oe.16.021773.
Debije, M.G., Verbunt, P.P.C., 2012. Thirty years of luminescent solar concentrator research: solar energy for the built environment. Adv. Energy. Mater. 2 (1), 12–35. https://doi.org/10.1002/aenm.201100554.
Kerrouche, A., et al., 2014. Luminescent solar concentrators: from experimental validation of 3D ray-tracing simulations to coloured stained-glass windows for BIPV. Sol. Energy Mater. Sol. Cells 122, 99–106. https://doi.org/10.1016/j.solmat.2013.11.026.
Sark, W.V., et al., 2017. The “electric mondrian” as a luminescent solar concentrator demonstrator case study. Solar RRL 1 (3–4), 1600015. https://doi.org/10.1002/solr.201600015.
Batchelder, J.S., et al., 1979. Luminescent solar concentrators. 1: Theory of operation and techniques for performance evaluation. Appl. Opt. 18 (18), 3090–3110. https://doi.org/10.1364/AO.18.003090.
Batchelder, J.S., et al., 1981. Luminescent solar concentrators. 2: Experimental and theoretical analysis of their possible efficiencies. Appl. Opt. 20 (21), 3733–3754. https://doi.org/10.1364/AO.20.003733.
Li, Y., et al., 2019. Review on the role of polymers in luminescent solar concentrators. J. Polym. Sci. A 57 (3), 201–215. https://doi.org/10.1002/pola.29192.
Debije, M.G., Rajkumar, V.A., 2015. Direct versus indirect illumination of a prototype luminescent solar concentrator. Sol. Energy 122, 334–340. https://doi.org/10.1016/j.solener.2015.08.036.
Li, Y., et al., 2019. Luminescent solar concentrators performing under different light conditions. Sol. Energy 188, 1248–1255. https://doi.org/10.1016/j.solener.2019.07.035.
Zhao, Y., Lunt, R.R., 2013. Transparent luminescent solar concentrators for large-area solar windows enabled by massive Stokes-shift nanocluster phosphors. Adv. Energy. Mater. 3 (9), 1143–1148. https://doi.org/10.1002/aenm.201300173.
Zhao, Y., et al., 2014. Near-Infrared harvesting transparent luminescent solar concentrators. Adv. Opt. Mater. 2 (7), 606–611. https://doi.org/10.1002/adom.201400103.
Yang, C., et al., 2018. Impact of stokes shift on the performance of near-infrared harvesting transparent luminescent solar concentrators. Sci. Rep. 8 (1), 16359. https://doi.org/10.1038/s41598-018-34442-3.
Chau, J.L.H., et al., 2010. Transparent solar cell window module. Sol. Energy Mater. Sol. Cells 94 (3), 588–591. https://doi.org/10.1016/j.solmat.2009.12.003.
Sanguineti, A., et al., 2013. High Stokes shift perylene dyes for luminescent solar concentrators. Chem. Commun. 49 (16), 1618–1620. https://doi.org/10.1039/c2cc38708e.
Mouedden, Y.E., et al., 2015. A cost-effective, long-lifetime efficient organic luminescent solar concentrator. J. Appl. Phys. 118, 015502. https://doi.org/10.1063/1.4923389.
Li, Y., et al., 2016. A structurally modified perylene dye for efficient luminescent solar concentrators. Sol. Energy 136, 668–674. https://doi.org/10.1016/j.solener.2016.07.051.
Purcell-Milton, F., Gun'ko, Y.K., 2012. Quantum dots for luminescent solar concentrators. J. Mater. Chem. 22 (33), 16687–16697. https://doi.org/10.1039/c2jm32366d.
Zhou, Y., et al., 2018. Harnessing the properties of colloidal quantum dots in luminescent solar concentrators. Chem. Soc. Rev. 47 (15), 5866–5890. https://doi.org/10.1039/c7cs00701a.
Moraitis, P., et al., 2018. Nanoparticles for luminescent solar concentrators – a review. Opt. Mater. 84, 636–645. https://doi.org/10.1016/j.optmat.2018.07.034.
Liu, C., et al., 2014. Luminescent solar concentrators fabricated by dispersing rare earth particles in PMMA waveguide. Int. J. Photoenergy 2014, 290952. https://doi.org/10.1155/2014/290952.
Freitas, V.T., et al., 2015. Eu^{3+}-based bridged silsesquioxanes for transparent luminescent solar concentrators. ACS Appl. Mater. Interfaces 7 (16), 8770–8778. https://doi.org/10.1021/acsami.5b01281.
Frias, A.R., et al., 2019. Transparent luminescent solar concentrators using Ln^{3+}-based ionosilicas towards photovoltaic windows. Energies 12 (3), 451. https://doi.org/10.3390/en12030451.
Shcherbatyuk, G.V., et al., 2010. Viability of using near infrared PbS quantum dots as active materials in luminescent solar concentrators. Appl. Phys. Lett. 96 (19), 191901. https://doi.org/10.1063/1.3422485.
Meinardi, F., et al., 2015. Highly efficient large-area colourless luminescent solar concentrators using heavy-metal-free colloidal quantum dots. Nat. Nanotechnol. 10, 878–885. https://doi.org/10.1038/nnano.2015.178.
Zhou, Y., et al., 2016. Near infrared, highly efficient luminescent solar concentrators. Adv. Energy. Mater. 6 (11), 1501913. https://doi.org/10.1002/aenm.201501913.
Sanguineti, A., et al., 2012. NIR emitting ytterbium chelates for colourless luminescent solar concentrators. Phys. Chem. Chem. Phys. 14 (18), 6452–6455. https://doi.org/10.1039/c2cp40791d.
Chen, W., et al., 2017. Heavy metal free nanocrystals with near infrared emission applying in luminescent solar concentrator. Solar RRL 1 (6), 1700041. https://doi.org/10.1002/solr.201700041.
Yang, C., et al., 2019. Integration of near-infrared harvesting transparent luminescent solar concentrators onto arbitrary surfaces. J. Luminescence 210, 239–246. https://doi.org/10.1016/j.jlumin.2019.02.042.
Wang, T., et al., 2011. Luminescent solar concentrator employing rare earth complex with

zero self-absorption loss. Sol. Energy 85 (11), 2571–2579. https://doi.org/10.1016/j.solener.2011.07.014.
Kate, O.M.T., et al., 2015. Efficient luminescent solar concentrators based on self-absorption free, Tm2+ doped halides. Sol. Energy Mater. Sol. Cells 140, 115–120. https://doi.org/10.1016/j.solmat.2015.04.002.
Meinardi, F., et al., 2017. Doped halide perovskite nanocrystals for reabsorption-free luminescent solar concentrators. ACS Energy Lett. 2 (10), 2368–2377. https://doi.org/10.1021/acsenergylett.7b00701.
Knowles, K.E., et al., 2015. Bright $CuInS_2$/CdS nanocrystal phosphors for high-gain full-spectrum luminescent solar concentrators. Chem. Commun. 51 (44), 9129–9132. https://doi.org/10.1039/c5cc02007g.
Zhang, B., et al., 2018. Aggregation-induced emission-mediated spectral downconversion in luminescent solar concentrators. Mater. Chem. Front. 2 (3), 615–619. https://doi.org/10.1039/c7qm00598a.
Bergren, M.R., et al., 2018. High-performance $CuInS_2$ quantum dot laminated glass luminescent solar concentrators for windows. ACS Energy Lett. 3 (3), 520–525. https://doi.org/10.1021/acsenergylett.7b01346.
Tseng, J.K., et al., 2011. Application of optical film with micro-lens array on a solar concentrator. Sol. Energy 85 (9), 2167–2178. https://doi.org/10.1016/j.solener.2011.06.004.
Damrongsak, P., Locharoenrat, K., 2017. Optical performance of fluorescent collectors integrated with microlens arrays. Mater. Res. Express 4 (9), 095502. https://doi.org/10.1088/2053-1591/aa8a1b.
Kurmi, I., et al., 2018. Micro-lens aperture array for enhanced thin-film imaging using luminescent concentrators. Opt. Express 26 (2), 29253–29261. https://doi.org/10.1364/oe.26.029253.
Chandra, S., et al., 2012. Enhanced quantum dot emission for luminescent solar concentrators using plasmonic interaction. Sol. Energy Mater. Sol. Cells 98, 385–390. https://doi.org/10.1016/j.solmat.2011.11.030.
Tummeltshammer, C., et al., 2013. Efficiency and loss mechanisms of plasmonic luminescent solar concentrators. Opt. Express 21 (S5), A735–A749. https://doi.org/10.1364/oe.21.00a735.
Fahad, M., et al., 2017. Metal nanoparticles based stack structured plasmonic luminescent solar concentrator. Sol. Energy 155, 934–941. https://doi.org/10.1016/j.solener.2017.07.037.
Debije, M.G., et al., 2010. Effect on the output of a luminescent solar concentrator on application of organic wavelength-selective mirrors. Appl. Opt. 49 (4), 745–751. https://doi.org/10.1364/ao.49.000745.
Verbunt, P.P., et al., 2012. Increased efficiency of luminescent solar concentrators after application of organic wavelength selective mirrors. Opt. Express 20 (S5), A655–A668. https://doi.org/10.1364/oe.20.00a655.
Connell, R., et al., 2018. Designing spectrally-selective mirrors for use in luminescent solar concentrators. J. Opt. 20 (2), 024009. https://doi.org/10.1088/2040-8986/aaa074.
Xu, L., et al., 2016. Enhanced photon collection in luminescent solar concentrators with distributed bragg reflectors. ACS Photonics 3 (2), 278–285. https://doi.org/10.1021/acsphotonics.5b00630.
Connell, R., Ferry, V.E., 2016. Integrating photonics with luminescent solar concentrators: optical transport in the presence of photonic mirrors. J. Phys. Chem. C 120 (37), 20991–20997. https://doi.org/10.1021/acs.jpcc.6b03304.
Iasilli, G., et al., 2019. Luminescent solar concentrators: boosted optical efficiency by polymer dielectric mirrors. Mater. Chem. Front. 3 (3), 429–436. https://doi.org/10.1039/c8qm00595h.
Vossen, F.M., et al., 2016. Visual performance of red luminescent solar concentrating windows in an office environment. Energy Build. 113, 123–132. https://doi.org/10.1016/j.enbuild.2015.12.022.
Corrado, C., et al., 2016. Power generation study of luminescent solar concentrator greenhouse. J. Renew. Sustain. Energy 8 (4), 043502. https://doi.org/10.1063/1.4958735.
Kanellis, M., et al., 2017. The solar noise barrier project: 1. Effect of incident light orientation on the performance of a large-scale luminescent solar concentrator noise barrier. Renew. Energy 103, 647–652. https://doi.org/10.1016/j.renene.2016.10.078.
Debije, M.G., et al., 2017. The solar noise barrier project: 2. The effect of street art on performance of a large scale luminescent solar concentrator prototype. Renew. Energy 113, 1288–1292. https://doi.org/10.1016/j.renene.2017.07.025.
Debije, M.G., et al., 2017. The solar noise barrier project: 3. The effects of seasonal spectral variation, cloud cover and heat distribution on the performance of full-scale luminescent solar concentrator panels. Renew. Energy 116A, 335–343. https://doi.org/10.1016/j.renene.2017.09.079.
Sutherland, B.R., 2018. Cost competitive luminescent solar concentrators. Joule 2 (2), 203–204. https://doi.org/10.1016/j.joule.2018.02.004.
Wilson, L.R., et al., 2010. Characterization and reduction of reabsorption losses in luminescent solar concentrators. Appl. Opt. 49 (9), 1651–1661. https://doi.org/10.1364/ao.49.001651.
Sala, P.D., et al., 2019. First demonstration of the use of very large Stokes shift cyclo-paraphenylenes as promising organic luminophores for transparent luminescent solar concentrators. Chem. Commun. 55 (21), 3160–3163. https://doi.org/10.1039/c8cc09859j.
Griffini, G., et al., 2013. Novel crosslinked host matrices based on fluorinated polymers for long-term durability in thin-film luminescent solar concentrators. Sol. Energy Mater. Sol. Cells 118, 36–42. https://doi.org/10.1016/j.solmat.2013.05.041.
Slooff, L.H., et al., 2008. A luminescent solar concentrator with 7.1% power conversion efficiency. Phys. Status Solidi RRL 2 (6), 257–259. https://doi.org/10.1002/pssr.200802186.
Sahin, D., et al., 2011. Monte-Carlo simulations of light propagation in luminescent solar concentrators based on semiconductor nanoparticles. J. Appl. Phys. 110 (3). https://doi.org/10.1063/1.3619809.
Leow, S.W., et al., 2013. Analyzing luminescent solar concentrators with front-facing photovoltaic cells using weighted Monte Carlo ray tracing. J. Appl. Phys. 113 (21). https://doi.org/10.1063/1.4807413.
Shu, J.P., et al., 2018. Monte-Carlo simulations of optical efficiency in luminescent solar concentrators based on all-inorganic perovskite quantum dots. Phys. B 548, 53–57. https://doi.org/10.1016/j.physb.2018.08.021.
Unit price of optical waveguide, https://www.plasticsinsight.com/resin-intelligence/resin-prices/pmma/, accessed on 6/5/2019.
Unit price of luminophores, https://www.tcichemicals.com/eshop/en/us/commodity/B4394/, accessed on 6/5/2019.
Unit price of solar cells, http://pvinsights.com/, accessed on 6/5/2019.